Enhanced quantitative X-ray phase-contrast images using Foucault differential filters

Jaeho Choi[1,*] and Young-Sung Park[1,2]

[1]*Department of Physics, Dankook University, Cheonan 31116, Korea*
[2]*Division of RI Convergence Research, Korea Institute of Radiological and Medical Sciences, Seoul 01812, Korea*
**Corresponding author: choi@dankook.ac.kr*

Received January 10, 2017; accepted May 18, 2017; posted online June 14, 2017

Enhanced quantitative X-ray phase-contrast (QXPC) imaging is implemented with a Foucault knife-edge array filter (FKAF), which is a real differential spatial filter. The intensities of Foucault differential filtering (FDF) are acquired according to the linear translation of the FKAF along the axes. The FDF using the FKAF scheme for obtaining the QXPC images is demonstrated by a stereoscopic rendering of the quantitative phase images of the tail fin of an anchovy containing soft and hard components in specimen. FDF is a noninterferometric quantitative phase-imaging method that depicts quantitative phase images and renders stereoscopic images.

OCIS codes: 110.7440, 180.7460, 100.5070, 070.6110.
doi: 10.3788/COL201715.081103.

Several X-ray phase visualization methods are being realized for imaging of phase objects, such as biological and polymeric specimens[1–3]. Grating-based phase-contrast imaging using a source-grating-attached X-ray tube that provides partially coherent X rays is one of the most successful methods in this field[4]. The propagation-based phase-contrast computed tomography has demonstrated samples containing both weakly and strongly absorbing biomedical materials[5]. Since the report of direct observation of thermal air turbulence using the Schlieren method, modifications of this technique have been used in fluid and aerodynamic research to depict the deviations of light beams induced by density gradients using an incoherent light source[6]. This improvement was accompanied by the development of spatial filters. The knife-edge test was reported for extraction of quantitative measurement of a nonsymmetric surface[7]. A phase-shift imaging method based on the multiline filter in the conventional Schlieren and phase-shift technique has been reported[8]. The Zernike-type phase-imaging method first used a filtering device evolved from knife-edge filters in visible light[9]. Thereafter, electron phase-contrast imaging was developed using this scheme[10,11]. However, this method could not be immediately applied to X-ray imaging, possibly because X-ray beams are intrinsically difficult to manipulate into highly coherent focused beams[12,13]. The X-ray Foucault knife-edge filtering method was demonstrated following the development of electron-phase imaging[14–16]. The achievement of quantitative phase imaging is one of the main topics in the field of X-ray imaging, especially regarding using a low flux and incoherent radiations source in the general laboratory environments. In this study, we report quantitative X-ray phase-contrast (QXPC) images generated using a Foucault differential filter (FDF) that was realized by the linear scanning of a Foucault knife-edge array filter (FKAF). The schematic diagram of the experimental setup is illustrated in Fig. 1.

It adopted the basic features of the Schlieren imaging apparatus, which uses an incoherent light source. A collimated beam is needed to perform spatial filtering. However, the spatial filtering in the hard X-ray region is restricted due to the generally low efficiency of X-ray collimation optics. In order to overcome the weakness of hard X-ray optics and to illuminate the partially collimated beam on the specimen, a pinhole array (PA) is utilized as an X-ray collimator. Then, an FKAF is exploited as

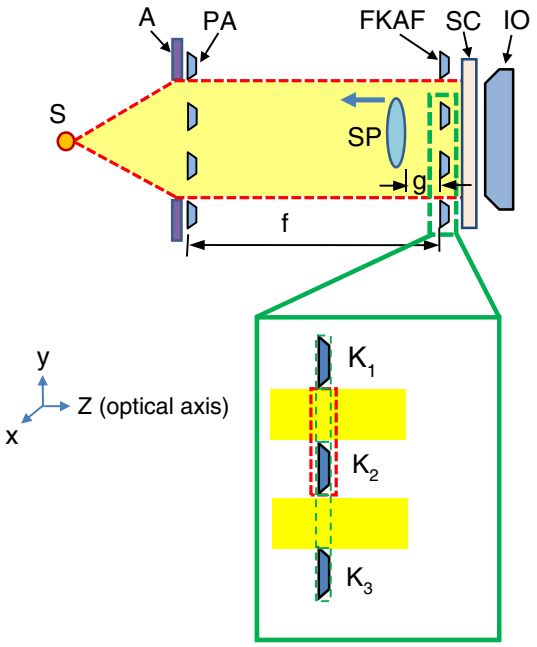

Fig. 1. (Color online) Schematic diagram of the FDF method. S, X-ray tube source; A, lead aperture; SC, scintillation crystal; IO, visible light imaging optics; SP, specimen; f, focal length of PA; g, distance between the end of the specimen surface and the FKAF; blue arrow, translation direction of SP. $k1$, $k2$, $k3$, knife edges; z axis, optical axis.

a derivative filter. In the region of interest (ROI) in Fig. 1 a partial view of the FKAF is depicted. The $k1$, $k2$, and $k3$ are representing a few of the knife-edge elements of the FKAF. The yellow rectangles represent the incoming X rays. In the ROI, the red-dotted line of the rectangle indicates a scan area of a knife-edge element in the data acquisition process. The scan process is illustrated in Fig. 2, considering the knife-edge element $k2$ is used to explicate the scan process. While the knife edges are moving to the positive y direction, the upper-positive scanning is defined by scanning the upper edge of $k2$ with transfer to the FKAF along the $+y$ direction [Fig. 2(a)]. The lower-positive scanning by the lower edge of $k2$ with the $+y$ direction scan are executed [Fig. 2(b)]. Thus, the relevant intensities of the upper-positive scan, $I_u(+y)$, and the lower-positive scan, $I_l(+y)$, are acquired with the $+y$ direction scan. The intensities $I_l(+y)$ are identical to $I_l(-y)$, which filtered the intensities by the lower knife edge, while moving in the negative y direction. The first derivative of the phase function is antisymmetric; thus, $I_l(-y) = -I_l(+y)$. Accordingly, these intensities, such as $I_u(+y)$ and $-I_l(+y)$, are acquired during the positive y-axis scanning. Consequently, the intensity difference of the positive and negative scans, i.e., $I_u(+y) - I_l(+y)$, can be concurrently detected by positive directional translation, and, unlike the conventional knife-edge scan, the orthogonal scanning is necessary. The identical process is applied to the x axis. The accumulated intensity out of the x- and y-axis scan becomes

$$I_a(r) = \sum_n [I_u(r) - I_l(r)], \tag{1}$$

where n is the scan numbers for the x and y axes, respectively, and $r = x, y$.

The data of FDF contains resultants of the Fourier transformation and the inverse Fourier transformation. Therefore, a further phase unwrapping process is not necessary to obtain phase-contrast images. The concept of imaging with the specimen translation along the optical axis is illustrated in Fig. 3. The image variation due to transporting the specimen along the optical axis caused by the angular ray deflection is given as $\alpha = (l/n_o)(\partial n/\partial z)$,

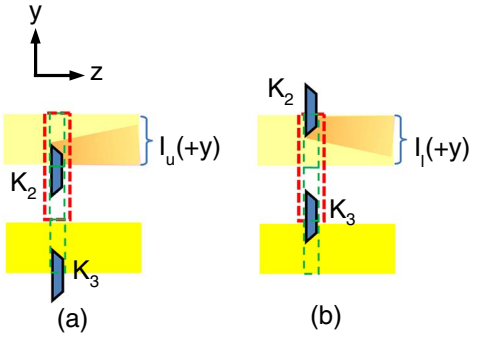

Fig. 2. Schematic of an example for the scan process to acquire FDF data in the xy plane by a knife-edge element $k2$.

where n_o, n are the refractive indices of the surroundings and the medium, respectively, and l is the length of the X-ray beam passes. The specific refracted beam is filtered by a certain knife-edge element of the FKAF. Consider two planes that are perpendicular to the optical ($z-$) axis in the specimen, the refractive index of surface $s1$ is smaller than $s2$. The partially collimated X rays are both transmitted through the planes in the in the specimen and refracted. The beam refracted ($r1$) from surface $s1$ is filtered by one of the FKAF elements, and the beam refracted ($r2$) from $s2$, which has a larger refractive index, is filtered by the other knife edge, as shown in Fig. 3(a). The distance $g1$ increases to $g2$ as result of the translation of the sample along the optical axis. The refracted beams ($r3$, $r4$), which have same angular ray deflection of $r1$ and $r2$, can be filtered by the identical knife edges that had filtered $r1$ and $r2$ because the straight line (SL) remains the same distance in Figs. 3(a) and 3(b). Consequently, the resultant QXPC images in the case of Figs. 3(a) and 3(b) are depicting different surfaces followed by the differential filtering of the xy plane shown and explained in Fig. 1.

The transmitted beams ($t1$–$t4$) are eventually eliminated in the imaging process because the differential filtering intensity (DFI) data acquired by the x- and y-axis scanning is divided by the total intensity of the transmitted beams[15,17]. The QXPC image of the xy plane at a certain position on the optical axis is given by

$$\left.\frac{\partial \varphi}{\partial r}\right|_z = \left.\frac{I_a(r)}{I_t(r)}\right|_z, \tag{2}$$

where $I_a(r)$ is sum of $I_u(r)$ and $I_l(r)$ acquired by the upper and lower knife edge of the FKAF, respectively. $I_t(r)$ is the transmission intensity.

In this experiment, the Au grid used as a PA was placed in front of the X-ray source after the lead aperture. The grid had hole dimensions of 7.5 μm × 7.5 μm and a bar width of 5.0 μm. Thus, the grid has the form of a knife-edge array with dimensions of 5.0 μm × 5.0 μm for each knife edge and the aspect ratio of 4:1. The FKAF, which

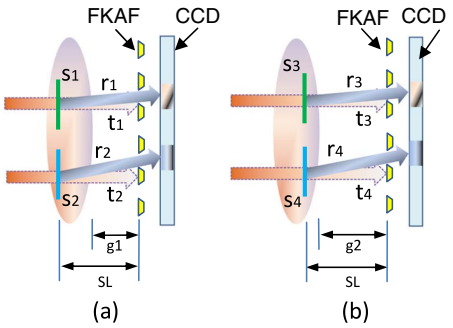

Fig. 3. Illustration of the concept of imaging the different surfaces using the FKA with optical axis translation of the specimen, $s1$–$s4$, surfaces in the specimen; $t1$–$t4$, transmitted X-rays; $r1$–$r4$, refracted X-rays.

has exactly same PA dimensions, was placed on the back focal plane of the PA. The focal length f was determined using the pinhole lens formula, i.e., $d \approx 1.9(f\lambda)^{1/2}$, where d is the pinhole diameter, and λ is the X-ray wavelength. The Cu target X-ray tube source was operated at an electric power of 43 kV/8.0 mA and emitted X rays with a wavelength of 1.54×10^{-10} m and a line focus of 4 mm × 8 mm. Thus, the corresponding back focal length of the PA was determined to be 101.2 mm. The images were acquired using an electron multiplying charge-coupled device (EMCCD) camera of the pixel size of 16 μm combined with a 150 μm-thick Ce doped YAG scintillation crystal and an optical microscope with a ×5 objective lens. Thus, the corresponding resolution of images is 3.2 μm. The distance between the PA and the scintillation crystal was 105.0 mm. A linear translator was installed on the experimental setup to scan the specimen along the optical axis. The distance (g) from the end surface of the specimen to the FKAF was ∼1 mm initially ($z = 0$). The transmission data were taken once the FKAF was pulled out from its set position. The DFIs were subsequently acquired to reposition the FKAF for five scans for each x- and y-axis combination (5×5 scans) with a scan step of 2.5 μm per step. The exposure time per scan was 100 s. QXPC images and stacked images were determined via simple arithmetic calculations using Eq. (2). Post-image rendering was performed using a public domain, Java-based image processing program ImageJ and the data visualization language, Interactive Data Language (IDL).

QXPC images of the tail fin of an anchovy are rendered to demonstrate the frequency domain adaptive filtering scheme. The specimen contains hard and soft tissues, and, thus, it is considered a proper material to depict the QXPC images for high- and low-absorption materials. Figure 4 shows a series of QXPC images, where z represents the specimen position along the optical axis every 250 μm intervals. Gradual variations of the images along the optical axis are shown for the parhypural (Ph) and hypurals (Hy) except for the upper preural centrumand (Pc). Although the caudal-fin ray, a thin transparent organ, was clearly visualized, the depth deviation is difficult to identify from each sectioning image. The surface rendering image, which is obtained by stacking the QXPC images along the z axis, can be depicted in the stereoscopic surface appearance, as shown in Fig. 5(a). Although the ROI [Fig. 5(b)], the upper bulging portion where the junction of the Pc and Ph dimmed in the images in Fig. 4 that were taken between $z = 0$ and 750 μm, its shape emerges clearly in the stereoscopic image. The cross-sectional view in Fig. 5(c) is cut along 10° and tilted relative to the xy plane in the ROI. It is shown that the bones are indicated at the junction of the Pc and Ph [Fig. 5(c2)]. Such cross-sectional views afford far more valuable data to determine the density distribution along the z axis than do intensity line profiles.

The QXPC imaging scheme is successfully demonstrated using the FKAF with an X-ray tube source with a low coherence and brilliance. In this method, the PA provides a proper coherency and surmount the low brilliancy of the source. We express the derivative filtering that obtained DFIs of the full field-of-view (FOV) diameter (3 mm) by only applying the scan range of 12.7 μm × 12.7 μm. It implies that the method needs a scanning length of only one period of FKAF to scan the full FOV. The image resolution can be increased as occasion demands, using the higher magnification of the objective lens. In post-processing, QXPC images are obtained through simple arithmetic calculations without the phase unwrapping process, in contrast to conventional phase-imaging methods. In addition, the density distributions, such as low-density materials (green, blue), are filled inside the bones. The overlapped phase can be recovered continuously without the 2π discontinuity, thus enabling imaging of a specimen that contains hard and soft materials. The presented scheme is a noninterferometric QXPC

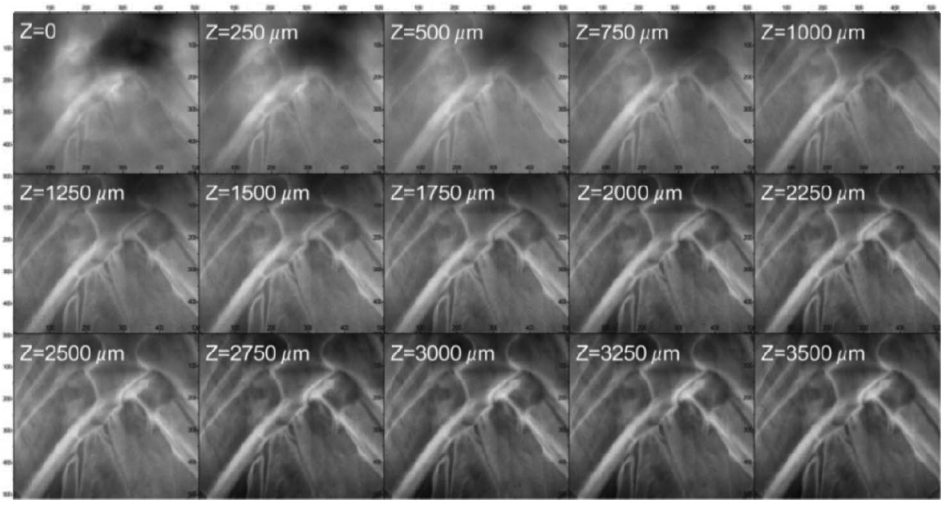

Fig. 4. Sequential QXPC images, where z represents the specimen position along the optical axis. The initial distance ($z = 0$) from the end surface of the specimen to the FKAF (g in Fig. 1) was ∼1 mm.

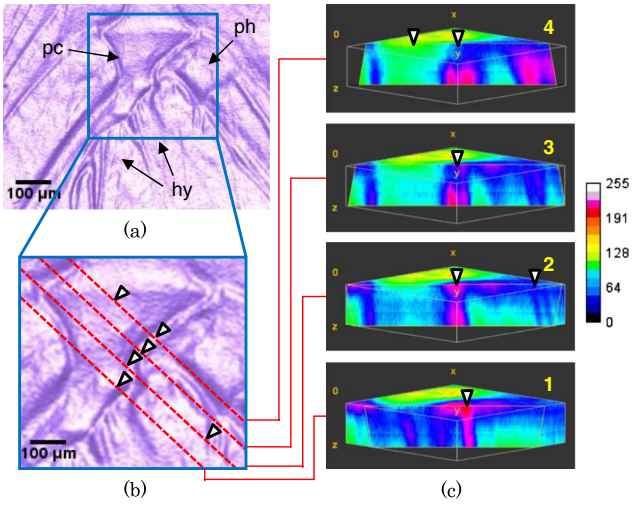

Fig. 5. (Color online) (a) Surface rendering image is depicted, using the stacked images of the QXPC. (b) ROI of a region of the upper Pc. Cross-sectional cut lines (red dots) rotated to $x = 76°$, $y = 45°$, and $z = 10°$ from their original axes. (c) Cross-sectional images along the cut lines. The arrow-heads at the cut lines on (c) represent the corresponding spots on the sliced planes on (c). The color bar expresses the relative intensity relevant to the density of the medium. Reddish and blue colors imply high- and low-density mediums, respectively.

imaging scheme that demonstrates enhanced quantitative phase-contrast images and feasibility of stereoscopic imaging by a linear translation of the sample or imaging devices. This scheme has a broad range of potential applications, such as an accurate bio-optic diagnosis of lesions and a nondestructive evaluation of electronic devices, in general laboratory environments using X-ray tube sources.

This work was supported by the research fund of Dankook University (No. R000122495).

References

1. Z. Huang, K. Kang, L. Zhang, Z. Chen, F. Ding, Z. Wang, and Q. Fang, Phys. Rev. A **79**, 013815 (2009).
2. J. Miao, T. Ishikawa, B. Johnson, E. H. Anderson, B. Lai, and K. O. Hodgson, Phys. Rev. Lett. **89**, 0883031 (2002).
3. B. E. Allman, P. J. McMahon, J. B. Tiller, K. A. Nugent, D. Paganin, and A. Barty, J. Opt. Soc. Am. A **17**, 1732 (2000).
4. C. David, J. Bruder, T. Rohbeck, C. Grünzweig, C. Kottler, A. Diaz, O. Bunk, and F. Pfeiffer, Microelectron. Eng. **84**, 1172 (2007).
5. H. Liu, Y. Ren, H. Guo, Y. Xue, H. Xie, T. Xiao, and X. Wu, Chin. Opt. Lett. **10**, 121101 (2012).
6. F. Devia, G. Milano, and G. Tanda, Exp. Therm. Fluid Sci. **8**, 1 (1994).
7. E. Gaviola, J. Opt. Soc. Am. **26**, 163 (1936).
8. L. Joannes, F. Dubois, and J. Legros, Appl. Opt. **42**, 5046 (2003).
9. F. Zernike, Phys. Zeitschr. **36**, 848 (1935).
10. K. Nagayama, J. Phys. Soc. Jpn. **73**, 2725 (2004).
11. R. Danev and K. Nagayama, Ultramicroscopy **88**, 243 (2001).
12. U. Neuhäusler, G. Schneider, W. Ludwig, M. A. Meyer, E. Zschech, and D. Hambach, J. Phys. D: Appl. Phys. **36**, A79 (2003).
13. C. Holzner, M. Feser, S. Vogt, B. Hornberger, S. Baine, and C. Jacobsen, Nat. Phys. **6**, 883 (2010).
14. N. Watanabe, T. Sasaya, Y. Imai, S. Iwata, K. Zama, and S. Aoki, *AIP Conf. Proc.* **2003**, 313 (2011).
15. J. Choi and Y. Park, Appl. Phys. Exp. **5**, 042503 (2012).
16. N. Watanabe, J. Hashizume, M. Goto, M Yamaguchi, T. Tsujiuura, and S. Aoki, J. Phys. Conf. Ser. **463**, 012011 (2013).
17. P. Hawkes, *Advances in Imaging and Electron Physics* (Elsevier Academic, 2005), Vol. **138**.